The H I Mass Function of the Local Universe: Combining Measurements from HIPASS, ALFALFA and FASHI

Wenlin Ma[1,2], Hong Guo[1], Haojie Xu[1], Michael G. Jones[3], Chuan-Peng Zhang[4,5], Ming Zhu[4,5], Jing Wang[6], Jie Wang[4], and Peng Jiang[4,5]

[1] Shanghai Astronomical Observatory, Chinese Academy of Sciences, Shanghai 200030, China. e-mail: `guohong@shao.ac.cn`
[2] University of Chinese Academy of Sciences, Beijing 100049, China. e-mail: `mawenlin@shao.ac.cn`
[3] Steward Observatory, University of Arizona, 933 N Cherry Ave., Tucson, AZ 85721, USA.
[4] National Astronomical Observatories, Chinese Academy of Sciences, Beijing 100101, China. e-mail: `cpzhang@nao.cas.cn`
[5] Guizhou Radio Astronomical Observatory, Guizhou University, Guiyang 550000, China. e-mail: `mz@nao.cas.cn`
[6] Kavli Institute for Astronomy and Astrophysics, Peking University, Beijing 100871, China.

November 18, 2024

ABSTRACT

We present the first H I mass function (HIMF) measurement for the recent FAST All Sky H I (FASHI) survey and the most complete measurements of HIMF in the local universe so far by combining the H I catalogues from H I Parkes All Sky Survey (HIPASS), Arecibo Legacy Fast ALFA (ALFALFA) and FASHI surveys at redshift $0 < z < 0.05$, covering 76% of the entire sky. We adopt the same methods to estimate distances, calculate sample completeness, and determine the HIMF for all three surveys. The best-fitting Schechter function for the total HIMF has a low-mass slope parameter $\alpha = -1.30 \pm 0.01$ and a 'knee' mass $\log(M_s/h_{70}^{-2}M_\odot) = 9.86 \pm 0.01$ and a normalisaztion $\phi_s = (6.58 \pm 0.23) \times 10^{-3} h_{70}^3 \, \text{Mpc}^{-3}\text{dex}^{-1}$. This gives the cosmic H I abundance $\Omega_{\text{H I}} = (4.54 \pm 0.20) \times 10^{-4} h_{70}^{-1}$. We find that a double Schechter function with the same slope α better describes our HIMF, and the two different 'knee' masses are $\log(M_{s_1}/h_{70}^{-2}M_\odot) = 9.96 \pm 0.03$ and $\log(M_{s_2}/h_{70}^{-2}M_\odot) = 9.65 \pm 0.07$. We verify that the measured HIMF is marginally affected by the choice of distance estimates. The effect of cosmic variance is significantly suppressed by combining the three surveys and it provides a unique opportunity to obtain an unbiased estimate of the HIMF in the local universe.

Key words. surveys – mass function – redshift and distance – radio lines

1. Introduction

Neutral hydrogen, in its atomic (H I) and molecular (H₂) forms, plays an important role in the baryon cycle of galaxies (see e.g., Péroux & Howk 2020; Saintonge & Catinella 2022, for reviews). Although H₂ is the direct fuel for star formation, H I serves as the reservoir to form H₂. Understanding the distribution of H I and how it is correlated with the properties of galaxies is crucial for theoretical studies of galaxy formation and evolution.

The two most important measurements for describing the H I content are the cosmic H I abundance ($\Omega_{\text{H I}}$) and the H I mass function (HIMF). $\Omega_{\text{H I}}$ quantifies the total H I mass in the universe and its evolution with redshift, $\Omega_{\text{H I}}(z)$, is closely related to the star formation history of galaxies (e.g., Rafieferantsoa et al. 2019; Kamphuis et al. 2022). As the counterpart of the galaxy stellar mass function in an optical survey, the HIMF describes the number densities of galaxies in different H I mass bins and provides the mass distribution of the H I gas in addition to the total abundance of $\Omega_{\text{H I}}$. In the local universe, $\Omega_{\text{H I}}$ can be accurately determined by directly summing up the HIMF. At higher redshifts, $\Omega_{\text{H I}}$ is usually estimated using the stacked H I signals and the damped Lyα systems, although with large uncertainties (see Péroux & Howk 2020, and references therein).

The HIMF is not only useful to derive $\Omega_{\text{H I}}$, but also encodes essential information about galaxy assembly histories. Since the H I gas distribution is very sensitive to accretion and feedback mechanisms (e.g. Fu et al. 2013; Popping et al. 2015; Xie et al. 2017; Guo et al. 2022), the HIMF serves as a valuable tool

to distinguish between various galaxy formation models, where the galaxy stellar mass functions at low redshifts are typically well reproduced (e.g., Baugh et al. 2019; Davé et al. 2020). The HIMF also shows a strong dependence on the halo and large-scale environment (e.g., Zwaan et al. 2005; Jones et al. 2020; Ma et al. 2024). Precise measurements of the HIMF are also the key science goal of current and future H I surveys, including the Widefield ASKAP L-band Legacy All-sky Blind Survey (WALLABY; Koribalski et al. 2020), the MeerKAT International GigaHertz Tiered Extragalactic Exploration (MIGHTEE; Jarvis et al. 2016), and the Five-hundred-meter Aperture Spherical radio Telescope (FAST) All Sky H I survey (FASHI; Zhang et al. 2024).

In the local universe ($z < 0.06$), the HIMF has been directly measured by the H I Parkes All-Sky Survey (HIPASS; Barnes et al. 2001; Meyer et al. 2004) and the Arecibo Fast Legacy ALFA Survey (ALFALFA; Giovanelli et al. 2005; Haynes et al. 2011). It has been found that the measured HIMF, $\phi(M_{\text{H I}})$, can be well described by a Schechter function (Schechter 1976),

$$\phi(M_{\text{H I}}) = \frac{dn}{d\log M_{\text{H I}}} = \ln(10)\phi_s \left(\frac{M_{\text{H I}}}{M_s}\right)^{\alpha+1} \exp\left(-\frac{M_{\text{H I}}}{M_s}\right), \quad (1)$$

where ϕ_s is the normalization, $\alpha + 1$ is the low-mass end slope, and M_s is the 'knee' mass.

Zwaan et al. (2005) used HIPASS and made one of the first HIMF measurements at $z \sim 0$, finding a 'knee' mass of $\log(M_s/h_{70}^{-2}M_\odot) = 9.80 \pm 0.03$ and a slope of $\alpha = -1.37 \pm 0.03$.

Using the 40% complete sample of ALFALFA that has much better sensitivity and resolution than HIPASS, Martin et al. (2010) found a higher 'knee' mass ($\log(M_s/h_{70}^{-2}M_\odot) = 9.96 \pm 0.02$) and a slightly flatter slope ($\alpha = -1.33 \pm 0.03$). The HIMF measurement was later updated by Jones et al. (2018) with the final ALFALFA sample, and they found a consistent 'knee' mass of $\log(M_s/h_{70}^{-2}M_\odot) = 9.94$, but a much shallower slope ($\alpha = -1.25 \pm 0.02$).

In optical surveys, galaxy stellar mass estimates may depend on various assumptions of initial mass functions, dust extinction laws, and stellar population synthesis models. The H I mass estimate of a target galaxy has the great advantage that it suffers from much less systematics and mainly depends on the uncertainties in the source distance (D_L) and the integrated H I line flux (S_{21}) (Meyer et al. 2017), as well as the unquantified self-absorption line. However, most blind H I surveys are not volume-limited in nature. The number of measured H I targets depends on both S_{21} and the width of the line profile (W_{50}). Galaxies with higher flux and narrower line profiles are much easier to detect (Giovanelli et al. 2005; Haynes et al. 2011). Therefore, it is crucial to quantify the sample completeness due to the selection effect. As shown in Guo et al. (2023), the differences between the HIMF measurements of Martin et al. (2010) and Jones et al. (2018) are caused by both cosmic variance and the adopted completeness cuts, where the 50% completeness cut is used in Jones et al. (2018), causing the shallower low-mass slope.

As investigated in Jones et al. (2018), the systematic uncertainties in the HIMF caused by distance estimates are very minor, only changing $\log M_s$ and α at the level of 0.01. The remaining source of systematic uncertainties, and likely the most important one when comparing the HIMFs of different surveys, is the cosmic variance effect. That is, the intrinsic HIMFs in different survey volumes, no matter how accurately they are measured, could vary from each other. This effect is already shown in the HIMF measurements of the final sample of ALFALFA. The differences between the separate measurements of α in the Spring and Fall sky regions of ALFALFA are 0.14, even when all other conditions are the same (see Fig. 3 of Jones et al. 2018). The apparent discrepancies between the HIMFs of HIPASS (southern sky) and ALFALFA (northern sky) could be caused by variations in galaxy populations and large-scale structures (Ma et al. 2024), as well as the different methods of estimating sample completeness and target distances.

However, galaxies with low H I masses can only be probed in a very limited redshift range, since the H I flux for a given H I mass would decrease rapidly as the distance increases ($S_{21} \propto D_L^{-2}$). To minimise the cosmic variance effect, we can increase the volume by conducting deeper H I surveys or covering a larger sky area. Recently, the first catalogue of the FASHI survey has been released (Zhang et al. 2024). It features significantly enhanced sensitivity, resolution and depth compared to previous surveys. This catalogue covers approximately 7600 square degrees of the sky, which is also complementary to the existing HIPASS and ALFALFA sky coverage. It offers an unprecedented opportunity to measure the most accurate HIMF in the local volume by combining the three survey catalogues.

In this paper, our aim is to measure the HIMF by combining the H I sources in the HIPASS, ALAFLFA and FASHI surveys, with a total sky coverage of around 31,528 deg² (i.e. nearly 76% of the entire sky). Most importantly, we will process all three catalogues using the same set of distance estimates, sample completeness corrections, and calculation method of HIMF. The resulting HIMF will provide an important reference for future H I surveys.

The organisation of this paper is as follows. In Section 2, we introduce the observational data used in the constraints. Section 3 describes the methods that we use in estimating HIMF. We show the results in Section 4. The discussion and conclusions are presented in Section 5 and Section 6, respectively. Throughout the paper, all masses are expressed in units of $M_\odot$. We adopt a flat ΛCDM cosmology of $\Omega_m = 0.3$ and the Hubble constant is assumed to be $H_0 = 70 \, h_{70} \, \mathrm{km \, s^{-1} \, Mpc^{-1}}$.

2. Data

In this work, we combine the HIPASS, ALFALFA and FASHI catalogues to measure the local HIMF at $0 < z < 0.05$. In Figure 1, we show the angular distributions of H I sources in FASHI (grey points in red regions), ALFALFA (grey points in blue regions) and HIPASS (grey points in yellow regions). In cases of overlaps between two surveys, we only adopt data from the survey with better sensitivity. Table 1 displays the details of the samples in three surveys, including the geometric cuts in the declination. We note that the sample size contains only galaxies above the 50% completeness limits (Section 3.2). The ranges of declination are determined to avoid overlap between the surveys.

2.1. HIPASS

HIPASS was carried out with the Parkes 64 m radio telescope in Australia. It is the first blind H I survey to cover the entire Southern sky with the declination ranging from $-90°$ to $+2°$ (Meyer et al. 2004). The HIPASS survey also has a northern extension catalogue covering the range of $+2° < \mathrm{Dec} < +25.5°$ (Wong et al. 2006), but it was not included in the HIMF calculation (Zwaan et al. 2005). It provides the largest uniform H I catalogue in the southern sky, with 4315 sources in the redshift range of $-1280 \mathrm{km \, s^{-1}} < cz_\odot < 12700 \mathrm{km \, s^{-1}}$. The Parkes beam diameter is 15.5 arcmin at 21 cm, and the rms noise of HIPASS is 13.3 mJy beam^{-1} at a velocity resolution of 26.4 km s^{-1}. As a first-generation survey, the mean depth of HIPASS was relatively shallow and it also suffers from a particularly large beam size (which can lead to source confusion and blending). In this paper, we limit the HIPASS sample to the declination range of $-90° < \mathrm{DEC} < 6.5°$ to avoid overlap with the FASHI south data.

2.2. ALFALFA

ALFALFA is a second-generation H I survey using the 305 m Arecibo single-dish telescope. Compared to HIPASS, ALFALFA has a much smaller beam diameter (3.8 arcmin at 21 cm) and the rms noise level is significantly improved (2.4 mJy per beam at a velocity resolution of 10 km s^{-1}). The final data release includes $\sim$ 31500 extragalactic sources and covers almost 6900 deg² of the northern sky in the redshift range of $-2000 \mathrm{km \, s^{-1}} < cz_\odot < 18000 \mathrm{km \, s^{-1}}$ (Haynes et al. 2018). The ALFALFA footprint is split into two continuous regions, which are name as the 'Spring Sky' ($07^h30^m < \mathrm{RA} < 16^h30^m$) and 'Fall Sky' ($22^h < \mathrm{RA} < 03^h$) according to their observation seasons. The declination ranges from 0° to 36° in both regions. A drift scan strategy was employed to observe both regions, resulting in high time efficiency and uniform coverage. In this paper, we only include the Code 1 sources (signal-to-noise ratio larger than 6.5) in the ALFALFA catalogue, as the reliability is close to 100% (Saintonge 2007). We follow the boundary cuts as in Jones et al. (2018) and limit the declination range to less than 30° to avoid overlap with FASHI. To be consistent with the HIMF mea-

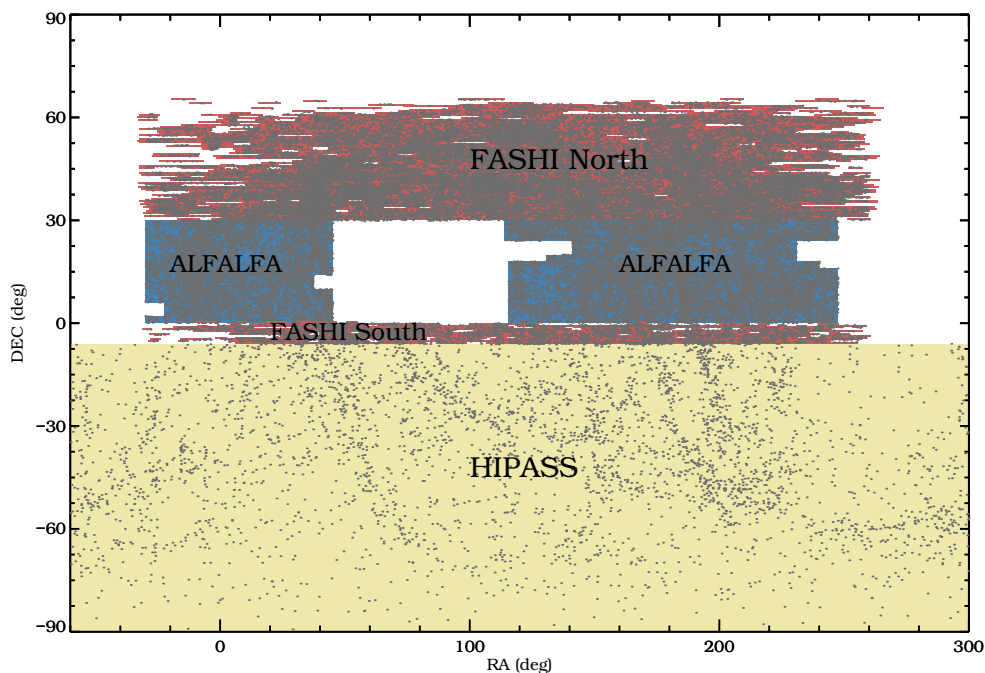Fig. 1: The angular distribution of H I sources in FASHI sky (red points points with grey areas), ALFALFA sky (blue points with grey areas) and HIPASS (black points with yellow areas) sky. As the sky coverage of FASHI survey is not uniform, we split it into several pixels, each with an area of 2 deg². In cases where there is an overlap between two surveys, we present the areas that have been surveyed deeper.

Table 1: The details of samples we adopted in three surveys.

Survey	z	Sample size	DEC range	Sky area (deg²)
HIPASS	0<z<0.042	3079	−90° < DEC < −6.5°	18291
ALFALFA	0<z<0.05	18713	0° < DEC < 30°	5649
FASHI North	0<z<0.05	16879	30° < DEC < 66°	5942
FASHI South	0<z<0.05	2720	−6.2° < DEC < 0°	1646

surement of Jones et al. (2018), we also limit the redshift range of ALFALFA to $0 < z < 0.05$, beyond which the radio frequency interference (RFI) becomes more severe.

2.3. FASHI

Base on the 500 m single-dish radio telescope FAST, FASHI has achieved a greater survey depth compared to both HIPASS and ALFALFA, as well as the smaller beam size (effectively 3.24 arcmin at 21 cm; Wang et al. 2023, 2024) and much lower rms noise level (1.5 mJy per beam at $6.4 \, \mathrm{km \, s^{-1}}$ resolution) (Zhang et al. 2024). FASHI was designed to observe the entire detectable sky of FAST in the declination range of $-14° < \mathrm{Dec} < +66°$ (around $22000 \, \mathrm{deg}^2$). The first data release (Zhang et al. 2024) covers two separate regions, which we call 'FASHI North' ($30° < \mathrm{DEC} < 66°$) and 'FASHI South' ($-6.2° < \mathrm{DEC} < 0°$), both with the right ascension in the ranges of $0^\mathrm{h} \leq \mathrm{RA} \leq 17.3^\mathrm{h}$ and $22^\mathrm{h} \leq \mathrm{RA} \leq 24^\mathrm{h}$. The observed redshift range of FASHI is $200 \mathrm{km \, s^{-1}} < cz_\odot < 26323 \mathrm{km \, s^{-1}}$ with the frequency range of 1305.5–1419.5 MHz. However, this frequency range includes radio recombination lines, which are produced by gas ionized by young, massive stars within H II regions of the Milky Way. To identify and eliminate these lines from the FASHI data, they used the criteria to ensure that the same spatial location exhibits consistent flux density and line width across various transition frequencies. In total, 41741 extragalactic sources have been detected. For fair comparisons with ALFALFA, we adopt the same redshift limits as $0 < z < 0.05$. Although FASHI observed quite a few galaxies in $0.05 < z < 0.09$, the influence of RFI there would be much more significant for our HIMF measurements.

Unlike ALFALFA, FASHI is carried out in a time-filler mode, i.e., the observations were made when there were no other running programs in the observing queue. This observation strategy made full use of the available time to increase the sample size, but results in an inhomogeneous survey depth. The sky areas sampled multiple times would be much deeper than in other regions. As shown in Fig. 5 of Zhang et al. (2024), the detection rms noise (in units of mJy per beam) varied strongly in different parts of the sky, as well as between FASHI North and FASHI South. FASHI South has a significantly higher detection rms noise, i.e. much lower source surface densities. Therefore, in this study, we treat FASHI North and FASHI South as two separate samples.

The problem of inhomogeneous sky coverage of FASHI is quite similar to the angular variations of observed galaxy surface number densities due to the foreground stars in optical surveys. Therefore, we follow the strategy of Xu et al. (2023) by applying correction weights to galaxies in different areas. To do this, we first split the FASHI sky coverage into grid pixels of equal area of $2 \, \mathrm{deg}^2$. Since the drift scans of FASHI were performed at a fixed

sky declination, we constructed the pixels in linear declination bins of $\Delta DEC = 0.5°$ and adjusted the number of RA bins in different DEC bins to reach the same pixel area. The resulting sky coverage of FASHI North and FASHI South is shown as the red regions in Figure 1. The distribution at the edge of the survey is discrete, but will be much improved in the future FASHI data release.

Then we calculate the normalised surface number density $\bar{n}/\bar{n}_{\text{total}}$ as a function of the median rms noise of the FASHI galaxies in each pixel, shown as the blue line in the left panel of Figure 2. $\bar{n}$ is the surface number density of galaxies in each pixel in per $\deg^2$ and $\bar{n}_{\text{total}}$ is the total surface number density in the whole sample. We adopt a quadratic relation to fit the rms noise dependence and assign each galaxy in a given pixel a weight of the reciprocal of the best-fitting quadratic function. We note that the weight assignment is pixel-wise, i.e. all galaxies in the same pixel share the same weight. So galaxies in the high surface density regions (i.e., low rms noise) are down-weighted to balance those in less-sampled regions. After applying this correction, the weighted source surface density is almost homogeneous (red line). The weights in different pixels for FASHI North are shown in the right panel of Figure 2. Most of the weights are in the range of 0.5–2 and we discard all pixels with weights larger than 2 to refrain from heavily weighting galaxies in less-sampled regions. The weights for FASHI North and FASHI South are calculated independently, based on their own galaxy samples.

3. Methods

The H I mass of each galaxy is determined from the flux following the standard equation (Meyer et al. 2017),

$$\frac{M_{\text{H I}}}{M_\odot} = \frac{2.356 \times 10^5}{1+z} \left(\frac{D_L(z)}{\text{Mpc}}\right)^2 \frac{S_{21}}{\text{Jy km s}^{-1}}, \tag{2}$$

where S_{21} is the integrated H I flux in units of Jy km s^{-1} and $D_L(z)$ is the luminosity distance to the galaxy in units of Mpc. In order to minimize the systematic uncertainties, we recalculate the H I mass in three catalogues in the same manner.

3.1. Distance Estimates

One of the main systematics of determining $M_{\text{H I}}$ is the uncertainties of $D_L(z)$. Pure Hubble flow distances are commonly used for $cz_\odot > 6000$km s^{-1} (Zwaan et al. 2005; Haynes et al. 2011), where the contribution of the peculiar velocity is relatively small. However, different flow models adopted to estimate peculiar velocities at $cz_\odot < 6000$km s^{-1} could potentially cause large systematic uncertainties in $D_L(z)$ (Masters et al. 2004). Masters (2005) proposed a Local Volume flow model to reduce the distance errors by considering the infall of galaxies onto local superclusters. But the distinct bias related to the line-of-sight galaxy density distribution, known as Malmquist bias (Lynden-Bell et al. 1988), will lead to incorrect assignment of peculiar velocities (Strauss & Willick 1995).

The Cosmicflows-4 Distance–Velocity Calculator (Kourkchi et al. 2020)[1] is designed to mitigate the Malmquist bias and the asymmetry in velocity errors in translations to distance from the logarithmic modulus. It is based on the Cosmicflows-4 catalogue (Tully et al. 2023) and consists of two calculators. One is based on the smoothed velocity field from the Numerical Action Methods (NAM; Shaya et al. 2017) model, but is only limited to a

distance of 38 Mpc. The other CF4 calculator is based on the Wiener filter model (Valade et al. 2024) and extends to 500 Mpc.

The original HIPASS catalogue used the pure Hubble flow distances (Meyer et al. 2004; Zwaan et al. 2005) and ALFALFA adopted a local volume flow model of Masters (2005) for $cz_\odot < 6000$km s^{-1}. FASHI used the NAM model of Cosmicflows-3 Distance–Velocity Calculator for $cz_\odot < 2400$km s^{-1} and the CF3 model (Graziani et al. 2019) for 2400km s$^{-1} < cz_\odot < 15000$km s^{-1} and the pure Hubble flow for $cz_\odot > 15000$km s^{-1}. In this paper, we apply the updated Cosmicflows-4 model of (Valade et al. 2024) to all three catalogues. As will be shown in Section 5.1, the influence of different flow models on the HIMF measurements in this study is minor.

3.2. Sample Completeness

The completeness of the H I sample is the main uncertainty in estimating the HIMF. One way to estimate completeness is to insert a large number of synthetic sources into the data. The completeness can then be determined from the rate of recovered synthetic sources (Rosenberg & Schneider 2002; Zwaan et al. 2004). In this study, we follow the method of Haynes et al. (2011) using the data themselves to calculate the completeness limits for three surveys. Since completeness is a function of both S_{21} and W_{50}, we divide $\log W_{50}$ into 20 bins from 1.0 to 3.0 with a bin width of 0.1. In each $\log W_{50}$ bin, we calculate the surface number density of galaxies in logarithmic intervals of S_{21}, $dn/d \log S_{21}$, as a function of $\log S_{21}$. The surface density, rather than the number of galaxies in each $\log S_{21}$ bin as in Fig. 11 of Haynes et al. (2011), is used for fair comparisons among samples from different survey areas.

We show the measurements of $S_{21}^{3/2} dn/d \log S_{21}$ in three representative $\log W_{50}$ bins in Figure 3. As discussed in Haynes et al. (2011), the galaxy surface density $dn/d \log S_{21}$ would be proportional to $S_{21}^{-3/2}$ for a complete sample. The deviation from a constant value of $S_{21}^{3/2} dn/d \log S_{21}$ marks the beginning of incompleteness. Following Haynes et al. (2011), we use an error function to fit the completeness $C(S_{21})$ in each W_{50} bin,

$$C(S_{21}) = \frac{1}{2} \left[1 + \text{erf}\left(\frac{\log S_{21} - \log S_{21,50\%}}{\sigma_{\log S_{21}}}\right) \right] \tag{3}$$

where the two free parameters are $S_{21,50\%}$ and $\sigma_{\log S_{21}}$. $S_{21,50\%}$ is the 50% completeness limit at a given W_{50} bin (i.e., $C(S_{21}) = 0.5$ when $S_{21} = S_{21,50\%}$), and $\sigma_{\log S_{21}}$ characterizes the slope of decreasing completeness at the low S_{21} end. In addition, we use a free parameter A_p to fit the plateau value of $S_{21}^{3/2} dn/d \log S_{21}$ in each W_{50} bin. The best-fitting curves are shown as solid lines in Figure 3. The 50% completeness limit $S_{21,50\%}$ in each W_{50} bin of FASHI North is shown as the vertical dotted line.

It is remarkable that ALFALFA, FASHI North and FASHI South share the same plateau value of $S_{21}^{3/2} dn/d \log S_{21}$ in each W_{50} bin, which demonstrates the reliability of the FASHI measurements. The HIPASS sample has consistently lower plateaus than other surveys, because it is limited to a smaller volume ($z < 0.042$ rather than $z < 0.05$) that causes lower surface densities. It is clear from the comparisons that FASHI North has the lowest rms noise, reaching a low flux density of $S_{21} \sim 0.1$Jy km s^{-1}, which is about 0.5 dex deeper than ALFALFA. HIPASS is considerably shallower than other surveys and is biased towards high S_{21} sources. ALFALFA and FASHI South have comparable survey depths, which validates our separate treatment of FASHI North and FASHI South.
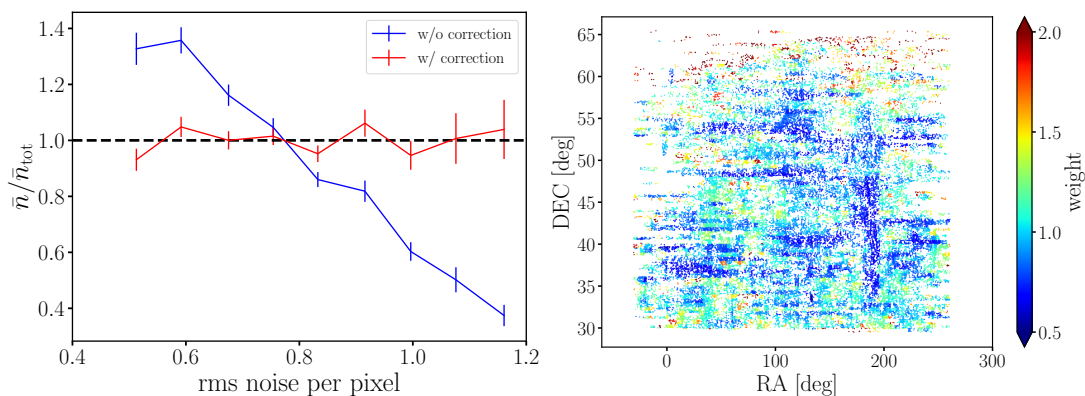
---

[1] https://edd.ifa.hawaii.edu/CF4calculator/

Fig. 2: The weight of FASHI North galaxies. Left panel: the blue line shows the normalised surface density as a function of the median rms noise of the FASHI galaxies in each pixel. And we weighted each galaxy with the reciprocal of the best-fitting rms noise dependence function to correct the surface density to be homogeneous, shown as red line. Right panel: the weights in different pixels for FASHI North. We only use pixels with the weights in the range of 0.5–2 to prevent assigning heavily weighting galaxies in less-sampled regions.
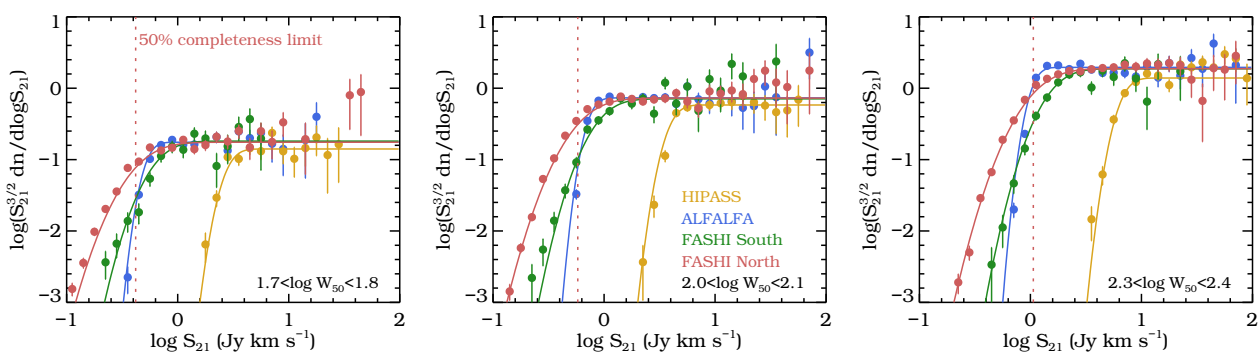

Fig. 3: Distribution of $S_{21}^{3/2} dn/d\log S_{21}$ as a function of the flux density S_{21}, where dn is the surface number density of galaxies in a given $\log S_{21}$ bin. This relation is used to determine the completeness of H I targets for all three surveys in different W_{50} bins, following the practice of Haynes et al. (2011). For fair comparisons, the measurements in both ALFALFA and FASHI are limited to the redshift range of $0 < z < 0.05$. But HIPASS only has the samples in $0 < z < 0.042$. The orange, blue, green and red circles are shown for the HIPASS, ALFALFA, FASHI South and FASHI North galaxies, respectively. The solid lines in each panel are the best-fitting error function. The vertical red dotted lines indicate the 50% completeness limit of FASHI North in each W_{50} bin.

In Figure 4, we show the dependence of $S_{21,50\%}$ on W_{50} as red circles for the four H I samples. The galaxy distribution in each sample is shown as the blue points. It is interesting that most galaxies in ALFALFA and HIPASS are above the 50% completeness limits. However, for FASHI north and FASHI south, there is still a large fraction of galaxies below the limits. This is related to the shallow slopes $\sigma_{\log S_{21}}$ in Figure 3. In Table 2, we list the numbers of galaxies above and below the 50% completeness cuts in the four samples. The fraction of galaxies below the cuts are about 17%, 9%, 45% and 34%, for HIPASS, ALFALFA, FASHI North, and FASHI South, respectively. Although FASHI is able to detect galaxies with low S_{21}, they are very incomplete. In order to avoid large corrections to low-completeness galaxies, we only use galaxies with $C(S_{21}) > 0.5$ to measure the HIMF. Currently, the fraction of discarded galaxies below the limits is quite large for FASHI, but it will be improved in future with better sampling rates.

As in Haynes et al. (2011), we also find that the function of $S_{21,50\%}(W_{50})$ can be well fitted with a broken power, as follows,

$$\log S_{21,50\%} = \begin{cases} 0.5 \log W_{50} - a_1 & \log W_{50} < W_{cut} \\ \log W_{50} - a_2 & \log W_{50} \geq W_{cut}, \end{cases} \quad (4)$$

where a_1 and a_2 are the free parameters. The transition W_{50} value, W_{cut}, is simply $2(a_2 - a_1)$. The best-fitting relations of the 50% completeness limits are shown as solid lines in Figure 4 and the parameters are listed in Table 2. Our derived values of a_1 and a_2 for ALFALFA differ slightly from those in Haynes et al. (2011) ($a_1 = 1.207$ and $a_2 = 2.457$), because their measurements were based on the early sample of 40% ALFALFA. Our values align well with those reported in Oman (2022) ($a_1 = 1.170$ and $a_2 = 2.420$), which also used the ALFALFA 100% sample.

3.3. Calculation Method of HIMF

To derive the HIMF, it is also necessary to know the detectable volume for each galaxy. The HIMF is commonly measured with the two-dimensional stepwise maximum likelihood (2DSWML) method (e.g., Efstathiou et al. 1988; Zwaan et al. 2005; Martin et al. 2010; Jones et al. 2018), by calculating the effective volume V_{eff} for each galaxy, which is often referred to as the $1/V_{eff}$ method. The effective volume is obtained by maximising the joint likelihood of finding all sample galaxies in different $M_{H I}$ and W_{50} bins. As extensively discussed in Martin et al. (2010), the $1/V_{eff}$ method has the advantage of being robust against density fluctuations in the large-scale structure, compared to the tra-

Table 2: The parameters in Equation 4 and the number of galaxies above and below 50% completeness in the four samples.

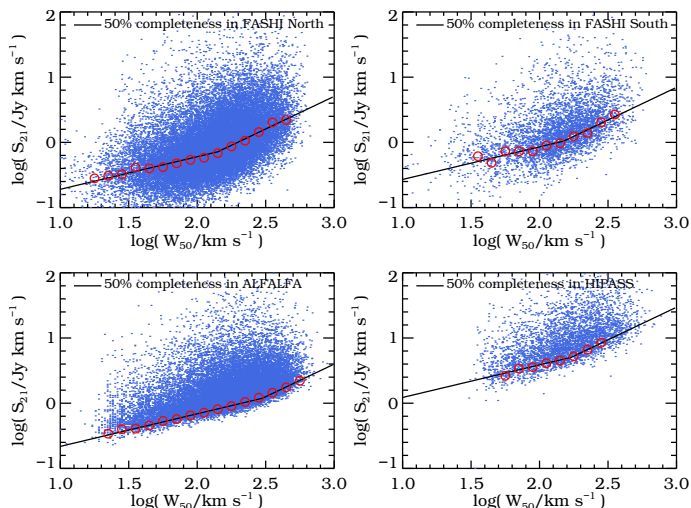| Survey	a_1	a_2	W_{cut}	$\sigma_{\log S_{21}}$	$S_{21} \geq S_{21,50\%}$	$S_{21} < S_{21,50\%}$
HIPASS	0.412	1.528	2.232	0.139	3079	649
ALFALFA	1.162	2.400	2.476	0.113	18713	1898
FASHI North	1.219	2.295	2.150	0.322	16879	13872
FASHI South	1.069	2.157	2.176	0.259	2720	1422

Fig. 4: Distribution of FASHI North (top left), FASHI South (top right), ALFALFA (bottom left) and HIPASS (bottom right) galaxies in the $\log S_{21}$–$\log W_{50}$ plane. Blue dots are all galaxy samples in each survey. Red open circles are the $\log S_{21}$ limit of 50% completeness in each $\log W_{50}$ bin. The black solid lines are the fitted broken power law relations.

ditional $1/V_{max}$ method (Schmidt 1968). It is also applied in a non-parametric way, i.e., without assuming a functional form of the HIMF.

However, the most important assumption of the $1/V_{eff}$ method is that the HIMF is universal for the whole volume of the survey. This is typically not valid for a large-volume survey. Even in the ALFALFA survey volume, large differences are present for the HIMFs of the Spring and Fall sky regions derived using the $1/V_{eff}$ method (see Fig. 3 of Jones et al. 2018). This method is not applicable in our study of combining the H ɪ measurements of three surveys covering substantially different large-scale structures. The other disadvantage of the $1/V_{eff}$ method is that it is very sensitive to the exact completeness cut. As shown in Fig. 1 of Oman (2022), the HIMF of ALFALFA measured with the $1/V_{eff}$ method is much higher at the low mass end by using a 0.02 dex higher $S_{21,50\%}$ cut from the ALFALFA 100% sample, compared to the old cut from the 40% sample.

The main bias in the $1/V_{max}$ method is the influence of large-scale structures. The ALFALFA volume covers the Virgo Cluster and the Local Supercluster, where the number densities of galaxies with low $M_{H\,ɪ}$ are much higher than those of other regions. The estimated HIMF using $1/V_{max}$ would be systematically overestimated at the low-mass end without corrections (Martin et al. 2010), which motivates the use of the $1/V_{eff}$ method in measuring the HIMF for ALFALFA. In this paper, by combining three surveys that cover almost 76% of the whole sky in the local universe, the influence of large-scale structures is effectively sup-

pressed. Therefore, we would adopt the $1/V_{max}$ method to measure the total HIMF.

The V_{max} value of each galaxy is simply obtained from the maximum distance that the galaxy can be observed with the 50% completeness limit. Since the HIPASS sample is limited to a slightly smaller redshift of $z < 0.042$, we assume that there is no evolution within the redshift range of $0.042 < z < 0.05$. The final HIMF can be obtain as,

$$\phi(M_{H\,ɪ}) = \sum_i \frac{1}{C(S_{21,i})V_{max,i}} \qquad (5)$$

where $C(S_{21,i})$ is the completeness of the i-th galaxy with a flux density $S_{21,i}$, and $V_{max,i}$ is the corresponding maximum volume. The sum is over all galaxies in a given $M_{H\,ɪ}$ bin. We note that $C(S_{21,i})$ also depends on W_{50} of the galaxy by the function of $S_{21,50\%}(W_{50})$. When combining the four samples, we calculate V_{max} for each galaxy using the total sky area of 31528 deg^2. We note that we only select galaxies above the 50% completeness cut and the incompleteness effect is taken into account in Equation 5 with the weight of $1/C(S_{21,i})$ for each galaxy.

4. H ɪ Mass Function

In the left panel of Figure 5, we show the total HIMF as open circles, along with the individual HIMFs of ALFALFA, HIPASS, FASHI North and FASHI South using solid lines of different colours. All measurements are listed in Table 3. The cosmic variance effect is weak for $M_{H\,ɪ} > 10^{10} M_\odot$, where the individual HIMFs of different samples are consistent with each other. These galaxies are probed to larger volumes, and thus less affected by the large-scale structures. But the discrepancies become much larger at the lower mass end, especially for $M_{H\,ɪ} < 10^8 M_\odot$. In fact, even for the deepest FASHI North sample, galaxies with $M_{H\,ɪ} < 10^8 M_\odot$ are only detected within 50 Mpc, which leads to the large variation of individual HIMFs at the low-mass end.

It is interesting that the HIMFs of ALFALFA and FASHI North are consistently higher than those of HIPASS and FASHI South for $M_{H\,ɪ} < 10^{10} M_\odot$. This reflects the differences in the large-scale structures of the northern and southern skies. As mentioned above, the superclusters in the northern sky will lead to the overestimate of the HIMF at the low mass end, while the voids presented in the southern sky will cause the underestimate, such as the Local Void (around RA~ 270° and DEC~ −30°) in the HIPASS footprint (Meyer et al. 2004). Combining the measurements in different surveys of various large-scale structures has significantly improved the estimates of the HIMF in the local universe.

For the total HIMF, the measurement errors would be less dominated by the cosmic variance effect, but rather by the Poisson noise caused by the limited numbers of galaxies. Therefore, we can approximate the variance for the total HIMF as in Jones
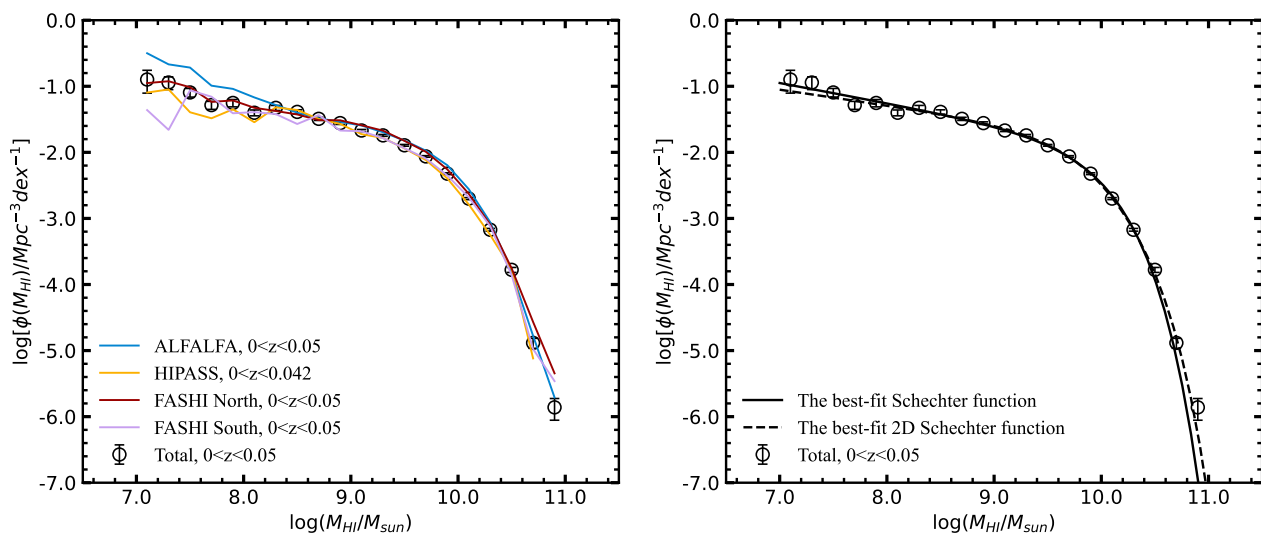
Fig. 5: Left: H I mass functions of ALFALFA, HIPASS, FASHI North and FASHI South, shown as blue, orange, red and purple solid lines, respectively. The total HIMF by combining three surveys is shown as black open circles with error bars. Right: the best-fit Schechter function (black solid line) and 2D Schechter function (black dashed lines).

et al. (2018),

$$\sigma^2(\phi) = \sum_i \left(\frac{1}{C(S_{21,i})V_{\max,i}} \right)^2 . \tag{6}$$

Following common practice, we also fit a Schechter function to the total HIMF, shown as the solid line in the right panel of Figure 5. The best-fitting parameters are $\alpha = -1.30 \pm 0.01$ and $\log(M_s/h_{70}^{-2}M_\odot) = 9.86 \pm 0.01$ and $\phi_s = (6.58 \pm 0.23) \times 10^{-3} h_{70}^3 \, \mathrm{Mpc}^{-3} \mathrm{dex}^{-1}$. The best-fitting parameters for the total HIMF and each of the three surveys are presented in Table 4. However, such a single Schechter fitting slightly underestimates the high-mass end of the HIMF (the largest H I mass bin). It has previously been suggested that a double Schechter function provides a much better fit to the galaxy stellar mass function at low redshifts, especially at the low mass end (see e.g., Baldry et al. 2008; Tomczak et al. 2014). We also adopt the following double-Schechter function to fit the total HIMF,

$$\begin{aligned}
\phi(M_{\mathrm{H\,I}}) =\ & \ln 10 \, \phi_{s_1} \left(\frac{M_{\mathrm{H\,I}}}{M_{s_1}} \right)^{\alpha+1} \exp\left(-\frac{M_{\mathrm{H\,I}}}{M_{s_1}} \right) \\
& + \ln 10 \, \phi_{s_2} \left(\frac{M_{\mathrm{H\,I}}}{M_{s_2}} \right)^{\alpha+1} \exp\left(-\frac{M_{\mathrm{H\,I}}}{M_{s_2}} \right),
\end{aligned} \tag{7}$$

where the parameters $(\phi_{s_1}, M_{s_1}, \alpha)$ and $(\phi_{s_2}, M_{s_2}, \alpha)$ are for the two Schechter components with the same slope α, respectively. Shown as dashed line in right panel of Figure 5, it fits better than single Schechter function, especially at the high-mass end. We find that the total HIMF is better fitted with the same slope α and two different 'knee' masses M_{s_1} and M_{s_2}. The best-fitting parameters are $\phi_{s_1} = (2.67 \pm 0.98) \times 10^{-3} h_{70}^3 \, \mathrm{Mpc}^{-3} \mathrm{dex}^{-1}$, $\log(M_{s_1}/h_{70}^{-2}M_\odot) = 9.96 \pm 0.03$, $\phi_{s_2} = (5.96 \pm 0.78) \times 10^{-3} h_{70}^3 \, \mathrm{Mpc}^{-3} \mathrm{dex}^{-1}$, $\log(M_{s_2}/h_{70}^{-2}M_\odot) = 9.65 \pm 0.07$, and $\alpha = -1.24 \pm 0.02$. The two different 'knee' masses are likely associated with different galaxy populations, e.g., central and satellite galaxies. It will be further confirmed in our future work with the decomposition of HIMF into central and satellite galaxies.

The cosmic H I abundance, $\Omega_{\mathrm{H\,I}}$, can be estimated by integrating the best-fitting single Schechter function as follows
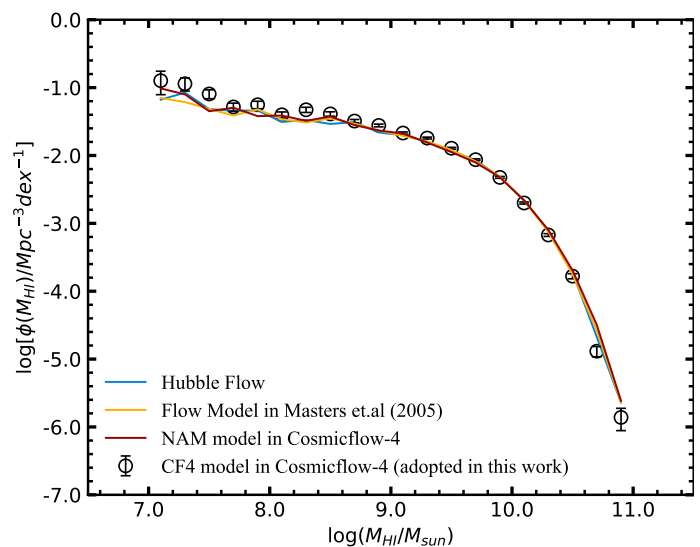

Fig. 6: The total H I mass functions calculated by different distance estimate models. The pure Hubble Flow, flow model in Masters (2005), NAM model and CF4 model in Cosmicflow-4 (adopted in our work) are shown as blue, orange, red solid lines and black open circles with errorbars, respectively.

(Martin et al. 2010; Jones et al. 2018),

$$\Omega_{\mathrm{H\,I}} = \frac{1}{\rho_c} \phi_s M_s \Gamma(\alpha + 2), \tag{8}$$

where ρ_c is the critical density at $z = 0$ (we assume $H_0 = 70 h_{70} \mathrm{km\,s^{-1}Mpc^{-1}}$). This gives $\Omega_{\mathrm{H\,I}} = (4.54 \pm 0.20) \times 10^{-4} h_{70}^{-1}$, which is almost the same for double Schechter function fits.

5. Discussion

5.1. Distance uncertainties

As discussed in previous sections, measurement errors in distance estimates could potentially lead to systematic uncertainties in the HIMF (Masters et al. 2004). In order to investigate

Table 3: The HIMF with errors of three surveys and the total results of their combination.

$\log(M_{\mathrm{H\,I}}/M_\odot)$	$\phi(M_{\mathrm{H\,I}})$ with errors (Mpc^{-3}dex^{-1})				
	HIPASS	ALFALFA	FASHI North	FASHI South	Total
7.1	$(8.036 \pm 8.036) \times 10^{-2}$	$(3.163 \pm 0.537) \times 10^{-1}$	$(1.118 \pm 0.255) \times 10^{-1}$	$(4.363 \pm 4.372) \times 10^{-2}$	$(1.266 \pm 0.479) \times 10^{-1}$
7.3	$(8.957 \pm 4.110) \times 10^{-2}$	$(2.147 \pm 0.350) \times 10^{-1}$	$(1.191 \pm 0.204) \times 10^{-1}$	$(2.192 \pm 1.676) \times 10^{-2}$	$(1.140 \pm 0.250) \times 10^{-1}$
7.5	$(4.045 \pm 1.852) \times 10^{-2}$	$(1.919 \pm 0.250) \times 10^{-1}$	$(9.678 \pm 1.408) \times 10^{-2}$	$(8.694 \pm 2.899) \times 10^{-2}$	$(8.063 \pm 1.204) \times 10^{-2}$
7.7	$(3.278 \pm 1.108) \times 10^{-2}$	$(1.022 \pm 0.151) \times 10^{-1}$	$(5.811 \pm 0.758) \times 10^{-2}$	$(6.954 \pm 1.831) \times 10^{-2}$	$(5.191 \pm 0.718) \times 10^{-2}$
7.9	$(4.486 \pm 1.172) \times 10^{-2}$	$(9.135 \pm 0.873) \times 10^{-2}$	$(6.103 \pm 0.595) \times 10^{-2}$	$(3.903 \pm 1.787) \times 10^{-2}$	$(5.593 \pm 0.713) \times 10^{-2}$
8.1	$(2.857 \pm 0.659) \times 10^{-2}$	$(6.782 \pm 0.544) \times 10^{-2}$	$(4.724 \pm 0.388) \times 10^{-2}$	$(4.067 \pm 0.860) \times 10^{-2}$	$(3.975 \pm 0.404) \times 10^{-2}$
8.3	$(4.807 \pm 0.695) \times 10^{-2}$	$(5.202 \pm 0.349) \times 10^{-2}$	$(4.227 \pm 0.285) \times 10^{-2}$	$(3.796 \pm 0.774) \times 10^{-2}$	$(4.716 \pm 0.413) \times 10^{-2}$
8.5	$(4.373 \pm 0.513) \times 10^{-2}$	$(3.989 \pm 0.226) \times 10^{-2}$	$(3.746 \pm 0.227) \times 10^{-2}$	$(2.687 \pm 0.380) \times 10^{-2}$	$(4.098 \pm 0.304) \times 10^{-2}$
8.7	$(3.203 \pm 0.295) \times 10^{-2}$	$(3.275 \pm 0.150) \times 10^{-2}$	$(3.078 \pm 0.143) \times 10^{-2}$	$(3.667 \pm 0.398) \times 10^{-2}$	$(3.217 \pm 0.177) \times 10^{-2}$
8.9	$(2.695 \pm 0.212) \times 10^{-2}$	$(2.899 \pm 0.106) \times 10^{-2}$	$(3.057 \pm 0.109) \times 10^{-2}$	$(2.139 \pm 0.197) \times 10^{-2}$	$(2.771 \pm 0.127) \times 10^{-2}$
9.1	$(1.884 \pm 0.131) \times 10^{-2}$	$(2.547 \pm 0.075) \times 10^{-2}$	$(2.569 \pm 0.078) \times 10^{-2}$	$(2.085 \pm 0.167) \times 10^{-2}$	$(2.142 \pm 0.079) \times 10^{-2}$
9.3	$(1.650 \pm 0.097) \times 10^{-2}$	$(2.019 \pm 0.050) \times 10^{-2}$	$(2.129 \pm 0.054) \times 10^{-2}$	$(1.641 \pm 0.102) \times 10^{-2}$	$(1.806 \pm 0.058) \times 10^{-2}$
9.5	$(1.149 \pm 0.064) \times 10^{-2}$	$(1.510 \pm 0.032) \times 10^{-2}$	$(1.494 \pm 0.034) \times 10^{-2}$	$(1.155 \pm 0.069) \times 10^{-2}$	$(1.279 \pm 0.038) \times 10^{-2}$
9.7	$(7.646 \pm 0.395) \times 10^{-3}$	$(1.060 \pm 0.020) \times 10^{-2}$	$(1.020 \pm 0.022) \times 10^{-2}$	$(8.062 \pm 0.463) \times 10^{-3}$	$(8.677 \pm 0.237) \times 10^{-3}$
9.9	$(4.032 \pm 0.250) \times 10^{-3}$	$(6.383 \pm 0.124) \times 10^{-3}$	$(5.525 \pm 0.130) \times 10^{-3}$	$(4.463 \pm 0.251) \times 10^{-3}$	$(4.757 \pm 0.150) \times 10^{-3}$
10.1	$(1.629 \pm 0.117) \times 10^{-3}$	$(2.773 \pm 0.064) \times 10^{-3}$	$(2.358 \pm 0.067) \times 10^{-3}$	$(2.085 \pm 0.144) \times 10^{-3}$	$(1.995 \pm 0.070) \times 10^{-3}$
10.3	$(5.612 \pm 0.524) \times 10^{-4}$	$(8.753 \pm 0.315) \times 10^{-4}$	$(8.044 \pm 0.327) \times 10^{-4}$	$(7.612 \pm 0.670) \times 10^{-4}$	$(6.737 \pm 0.317) \times 10^{-4}$
10.5	$(1.703 \pm 0.240) \times 10^{-4}$	$(1.543 \pm 0.125) \times 10^{-4}$	$(1.754 \pm 0.133) \times 10^{-4}$	$(1.386 \pm 0.230) \times 10^{-4}$	$(1.667 \pm 0.144) \times 10^{-4}$
10.7	$(7.614 \pm 3.232) \times 10^{-6}$	$(1.670 \pm 0.405) \times 10^{-5}$	$(2.709 \pm 0.506) \times 10^{-5}$	$(1.055 \pm 0.611) \times 10^{-5}$	$(1.307 \pm 0.225) \times 10^{-5}$
10.9	-	$(1.951 \pm 1.380) \times 10^{-6}$	$(4.523 \pm 2.095) \times 10^{-6}$	$(3.448 \pm 3.434) \times 10^{-6}$	$(1.382 \pm 0.499) \times 10^{-6}$

Table 4: HIMF fit parameters for three surveys and the total results of their combination.

Survey	α	$\log(M_s/h_{70}^{-2}M_\odot)$	$\phi_s/h_{70}^3\mathrm{Mpc}^{-3}\mathrm{dex}^{-1}$
Total	-1.30 ± 0.01	9.86 ± 0.01	$(6.58 \pm 0.23) \times 10^{-3}$
HIPASS	-1.28 ± 0.02	9.83 ± 0.02	$(6.37 \pm 0.42) \times 10^{-3}$
ALFALFA	-1.29 ± 0.01	9.87 ± 0.01	$(7.91 \pm 0.22) \times 10^{-3}$
FASHI North	-1.26 ± 0.01	9.84 ± 0.01	$(8.26 \pm 0.24) \times 10^{-3}$
FASHI South	-1.25 ± 0.03	9.86 ± 0.02	$(6.36 \pm 0.43) \times 10^{-3}$

the effect of distance estimates, we follow the practice of Jones et al. (2018) to measure the HIMFs by applying different flow models. In Figure 6, we compare the total HIMFs calculated using different distance models, including the pure Hubble flow (blue line, assuming $H_0 = 70h_{70}\mathrm{km\,s^{-1}Mpc^{-1}}$), the flow model of Masters (2005) (orange line), the NAM model (red line) and the CF4 model (adopted in this work) in the Cosmicflows-4 Distance–Velocity Calculator. The distance estimates in the NAM model are limited to 38 Mpc, whereas the CF4 model extends this limit to 500 Mpc. The flow model of Masters (2005) is also limited to a distance of $cz_\odot < 6000\mathrm{km\,s^{-1}}$ as in the ALFALFA sample. For galaxies lying beyond these distances, we utilised the pure Hubble flow.

The HIMF with the CF4 model is consistent with all other models for $M_{\mathrm{H\,I}} > 10^9 M_\odot$, but is slightly higher at the low mass end. As shown in Tully et al. (2023), by including the kinematic information of ALFALFA, the peculiar velocities in Cosmicflows-4 is much improved compared to Cosmicflows-3. The maximum difference in these distance estimates for $M_{\mathrm{H\,I}} < 10^8 M_\odot$ is around $\Delta \log D_L \sim 0.08$, which will introduce an offset

of 0.16 dex in the H I mass at the low-mass end. Since the HIMF at the low-mass end is $\phi(M_{\mathrm{H\,I}}) \propto M_{\mathrm{H\,I}}^{\alpha+1}$, the 0.16 dex offset in $M_{\mathrm{H\,I}}$ will translate to a minor offset of 0.048 dex in $\phi(M_{\mathrm{H\,I}})$ for $\alpha = -1.30$. The small number of galaxies at the low-mass end also limits our ability to tightly constrain the HIMF here. For the massive end, the effects of different flow models are weaker with respect to the pure Hubble flow. Therefore, we conclude that the effect of different distance estimates would not substantially change the measured HIMF, consistent with the results shown in Jones et al. (2018).

5.2. Comparison with literature

In Figure 7, we compare our HIMF measurement (open circles) with those of HIPASS from Zwaan et al. (2005), ALFALFA from Guo et al. (2023), the Arecibo Ultra-Deep Survey (AUDS) from Xi et al. (2021) and the MIGHTEE-HI of Ponomareva et al. (2023).

The HIMF of HIPASS in Zwaan et al. (2005) shows a slightly lower high-mass end amplitude. For fair comparisons, we have

simply corrected for the differences in their $M_{H\,I}$ and $\phi(M_{H\,I})$ definitions of $H_0 = 75h_{75}\,\mathrm{km\,s^{-1}Mpc^{-1}}$ by a 0.06 dex increase in $M_{H\,I}$ and -0.09 dex decrease in $\phi(M_{H\,I})$. However, the definition of $M_{H\,I}$ will also affect the completeness estimates. They also adopted a different completeness estimation method using the recovered rates of inserted synthetic sources, as described in Zwaan et al. (2004). The underestimate of $\phi(M_{H\,I})$ at the high mass end could be caused by differences in the completeness function and the estimation of the overall normalisation in the 2DSWML method (Zwaan et al. 2003).

The HIMF measurement of Guo et al. (2023) used the ALFALFA 100% sample and corrected for the incompleteness effect in Jones et al. (2018) by using the 90% completeness cut $S_{21,90\%}$ of Haynes et al. (2011). Their HIMF and $\Omega_{H\,I} = (4.55 \pm 0.29) \times 10^{-4} h_{70}^{-1}$ are quite consistent with our results. We also show the AUDS measurement of Xi et al. (2021) that extends to a slightly higher redshift of $z = 0.16$. It shows a mild redshift evolution of the HIMF, with a shallower slope at the high-mass end. However, their H I detection only included 247 galaxies in a sky area of $1.35\,\mathrm{deg}^2$. The small number of galaxies limits an accurate determination of the HIMF. But they found $\Omega_{H\,I} = (3.93 \pm 0.68) \times 10^{-4} h_{70}^{-1}$, consistent with our $\Omega_{H\,I}$ measurement. Ponomareva et al. (2023) measured the HIMF using the MIGHTEE-HI survey in a redshift range of $0 \leq z \leq 0.084$. They also found slightly higher $\phi(M_{H\,I})$ at $M_{H\,I} > 10^{10} M_\odot$ than the $z = 0$ measurements. Their $\Omega_{H\,I}$ measurement is slightly larger, with $\Omega_{H\,I} = 5.46^{+0.94}_{-0.99} \times 10^{-4} h_{67.4}^{-1}$, albeit with large errors. These measurements tend to point to the weak evolution of $\Omega_{H\,I}$ in $0 < z < 0.2$ (Rhee et al. 2018; Walter et al. 2020), consistent with the prediction of the theoretical model (Guo et al. 2023). Ongoing and future deep H I observations, e.g., the FAST Ultra-Deep Survey (Xi et al. 2024), will provide more insight on the evolution of HIMF.

We note that the HIMF of our total sample is consistent with the HIMF of Guo et al. (2023). But from the best-fitting Schechter function fits displayed in Table 4, the relevant fitting parameters are slightly different. We have a slightly lower 'knee' mass of $\log(M_s/h_{70}^{-2} M_\odot) = 9.86 \pm 0.01$, while it is $\log(M_s/h_{70}^{-2} M_\odot) = 9.91 \pm 0.01$ in Guo et al. (2023). However, as shown in Fig. 4 of Ponomareva et al. (2023), the three parameters of the Schechter function are strongly correlated with each other, with M_s showing anti-correlations with α and ϕ_s. The comparisons between the parameters of Schechter function fits of different samples should not be treated independently.

6. Conclusions

In this study, we measure the H I mass function in the local universe ($0 < z < 0.05$) by combining the H I samples in the HIPASS, ALFALFA and FASHI surveys, covering 76% of the entire sky ($31528\,\mathrm{deg}^2$). The combined sample has the advantage of greatly suppressing the influence of cosmic variance on the measured HIMF. To further reduce systematic uncertainties in the processing of the H I catalogues, we adopted the same methods to estimate distances, calculate sample completeness, and determine the HIMF (the $1/V_{\max}$ method) for all three catalogues. We measured the most complete HIMF in the local universe so far (Figure 5) and also presented the first HIMF measurement for the recent FASHI survey.

We fitted the total HIMF with a single Schechter function, with the parameters of $\alpha = -1.30 \pm 0.01$ and $\log(M_s/h_{70}^{-2} M_\odot) = 9.86 \pm 0.01$ and $\phi_s = (6.58 \pm 0.23) \times 10^{-3} h_{70}^3\,\mathrm{Mpc^{-3}dex^{-1}}$. The derived cosmic H I abundance is $\Omega_{H\,I} = (4.54 \pm 0.20) \times 10^{-4} h_{70}^{-1}$,
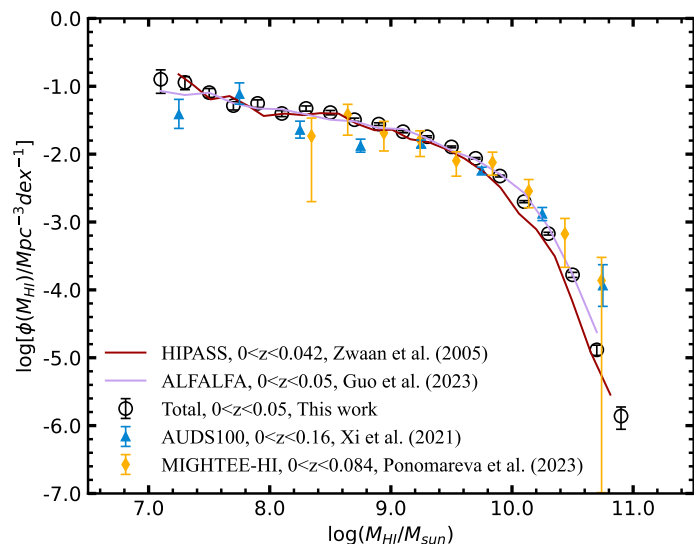

Fig. 7: The comparisons of HIMF in different works. Measurements of HIPASS in Zwaan et al. (2005), ALFALFA in Guo et al. (2023), AUDS100 in Xi et al. (2021) and MIGHTEE–HI in Ponomareva et al. (2023) are shown as red solid line, purple solid line, blue triangles and yellow diamonds, respectively. The total HIMF in this work is shown as black open circles with error bars.

which is consistent with the measurement using the ALFALFA 100% complete sample (Guo et al. 2023). However, we find that our HIMF is better described by a double Schechter function with the same slope α. The best-fitting parameters are $\phi_{s_1} = (2.67 \pm 0.98) \times 10^{-3} h_{70}^{-2}\,\mathrm{Mpc^{-3}dex^{-1}}$, $\log(M_{s_1}/h_{70}^{-2} M_\odot) = 9.96 \pm 0.03$, $\phi_{s_2} = (5.96 \pm 0.78) \times 10^{-3} h_{70}^3\,\mathrm{Mpc^{-3}dex^{-1}}$, $\log(M_{s_2}/h_{70}^{-2} M_\odot) = 9.65 \pm 0.07$, and $\alpha = -1.24 \pm 0.02$. The two different 'knee' masses are favoured by the measured HIMF at the massive end, indicating contributions from two different components (likely from the central and satellite galaxies).

We found that the measured HIMF is marginally affected by the choice of distance estimates. We adopted different flow models to estimate the luminosity distances and obtained very consistent results. However, the local large-scale structures have a strong influence on the HIMF when measured separately in different H I samples, especially at the low-mass end. ALFALFA and FASHI North have consistently higher HIMFs than those of HIPASS and FASHI South, due to the influence of local superclusters. Combining the three H I surveys provides the unique opportunity to obtain an unbiased estimate of the HIMF in the local universe.

Although the combined sample covers a large sky area, galaxies with low $M_{H\,I}$ are still probed within very limited volumes and a limited number of statistics. Future deeper H I surveys will provide more robust measurements of HIMF at the low mass end.

Acknowledgements

References

Baldry, I. K., Glazebrook, K., & Driver, S. P. 2008, MNRAS, 388, 945
Barnes, D. G., Staveley-Smith, L., de Blok, W. J. G., et al. 2001, MNRAS, 322, 486
Baugh, C. M., Gonzalez-Perez, V., Lagos, C. d. P., et al. 2019, MNRAS, 483, 4922
Davé, R., Crain, R. A., Stevens, A. R. H., et al. 2020, MNRAS, 497, 146
Efstathiou, G., Ellis, R. S., & Peterson, B. A. 1988, MNRAS, 232, 431
Fu, J., Kauffmann, G., Huang, M.-l., et al. 2013, MNRAS, 434, 1531
Giovanelli, R., Haynes, M. P., Kent, B. R., et al. 2005, AJ, 130, 2598
Graziani, R., Courtois, H. M., Lavaux, G., et al. 2019, MNRAS, 488, 5438
Guo, H., Jones, M. G., & Wang, J. 2022, ApJ, 933, L12
Guo, H., Wang, J., Jones, M. G., & Behroozi, P. 2023, ApJ, 955, 57
Haynes, M. P., Giovanelli, R., Kent, B. R., et al. 2018, ApJ, 861, 49
Haynes, M. P., Giovanelli, R., Martin, A. M., et al. 2011, AJ, 142, 170
Jarvis, M., Taylor, R., Agudo, I., et al. 2016, in MeerKAT Science: On the Pathway to the SKA, 6
Jones, M. G., Haynes, M. P., Giovanelli, R., & Moorman, C. 2018, MNRAS, 477, 2
Jones, M. G., Hess, K. M., Adams, E. A. K., & Verdes-Montenegro, L. 2020, MNRAS, 494, 2090
Kamphuis, P., Jütte, E., Heald, G. H., et al. 2022, A&A, 668, A182
Koribalski, B. S., Staveley-Smith, L., Westmeier, T., et al. 2020, Ap&SS, 365, 118
Kourkchi, E., Courtois, H. M., Graziani, R., et al. 2020, AJ, 159, 67
Lynden-Bell, D., Faber, S. M., Burstein, D., et al. 1988, ApJ, 326, 19
Ma, W., Guo, H., & Jones, M. G. 2024, arXiv e-prints, arXiv:2409.08539
Martin, A. M., Papastergis, E., Giovanelli, R., et al. 2010, ApJ, 723, 1359
Masters, K. L. 2005, PhD thesis, Cornell University, New York
Masters, K. L., Haynes, M. P., & Giovanelli, R. 2004, ApJ, 607, L115
Meyer, M., Robotham, A., Obreschkow, D., et al. 2017, PASA, 34, 52
Meyer, M. J., Zwaan, M. A., Webster, R. L., et al. 2004, MNRAS, 350, 1195
Oman, K. A. 2022, MNRAS, 509, 3268
Péroux, C. & Howk, J. C. 2020, ARA&A, 58, 363
Ponomareva, A. A., Jarvis, M. J., Pan, H., et al. 2023, MNRAS, 522, 5308
Popping, G., Caputi, K. I., Trager, S. C., et al. 2015, MNRAS, 454, 2258
Rafieferantsoa, M., Davé, R., & Naab, T. 2019, MNRAS, 486, 5184
Rhee, J., Lah, P., Briggs, F. H., et al. 2018, MNRAS, 473, 1879
Rosenberg, J. L. & Schneider, S. E. 2002, ApJ, 567, 247
Saintonge, A. 2007, AJ, 133, 2087
Saintonge, A. & Catinella, B. 2022, ARA&A, 60, 319
Schechter, P. 1976, ApJ, 203, 297
Schmidt, M. 1968, ApJ, 151, 393
Shaya, E. J., Tully, R. B., Hoffman, Y., & Pomarède, D. 2017, ApJ, 850, 207
Strauss, M. A. & Willick, J. A. 1995, Phys. Rep., 261, 271
Tomczak, A. R., Quadri, R. F., Tran, K.-V. H., et al. 2014, ApJ, 783, 85
Tully, R. B., Kourkchi, E., Courtois, H. M., et al. 2023, ApJ, 944, 94
Valade, A., Libeskind, N. I., Pomarède, D., et al. 2024, Nature Astronomy [arXiv:2409.17261]
Walter, F., Carilli, C., Neeleman, M., et al. 2020, ApJ, 902, 111
Wang, J., Lin, X., Yang, D., et al. 2024, ApJ, 968, 48
Wang, J., Yang, D., Oh, S. H., et al. 2023, ApJ, 944, 102
Wong, O. I., Ryan-Weber, E. V., Garcia-Appadoo, D. A., et al. 2006, MNRAS, 371, 1855
Xi, H., Peng, B., Staveley-Smith, L., et al. 2024, ApJS, 274, 18
Xi, H., Staveley-Smith, L., For, B.-Q., et al. 2021, MNRAS, 501, 4550
Xie, L., De Lucia, G., Hirschmann, M., Fontanot, F., & Zoldan, A. 2017, MNRAS, 469, 968
Xu, H., Zhang, P., Peng, H., et al. 2023, MNRAS, 520, 161
Zhang, C.-P., Zhu, M., Jiang, P., et al. 2024, Science China Physics, Mechanics, and Astronomy, 67, 219511
Zwaan, M. A., Meyer, M. J., Staveley-Smith, L., & Webster, R. L. 2005, MNRAS, 359, L30
Zwaan, M. A., Meyer, M. J., Webster, R. L., et al. 2004, MNRAS, 350, 1210
Zwaan, M. A., Staveley-Smith, L., Koribalski, B. S., et al. 2003, AJ, 125, 2842